SUPPLEMENTARY INFORMATION

Broadband evolution of phononic-crystal-waveguide eigenstates in real- and k-spaces

P. H. Otsuka, K. Nanri, O. Matsuda, M. Tomoda, and D. M. Profunser
Division of Applied Physics, Faculty of Engineering, Hokkaido University, Sapporo, 060-8628, Japan

I. A. Veres
Recendt, Research Center for Non-Destructive Testing GmbH, Altenberger Str. 69, 4040 Linz, Austria

S. Danworaphong
School of Science, Walailak University, Nakhon Si Thammarat, 80160, Thailand

A. Khelif, S. Benchabane, and V. Laude
Institut FEMTO-ST, Université de Franche-Comté and CNRS,
32 Avenue de l'Observatoire, F-25044, Besançon, France

O. B. Wright
Division of Applied Physics, Faculty of Engineering, Hokkaido University, Sapporo, 060–8628, Japan

This Supplementary Information contains details of the Fourier analysis in **k**-t space, the simulation method for the straight and L waveguides, the animations in real space, **k**-t space and energy space, including simulations, the spatiotemporal Fourier analysis and acoustic frequency spectrum, the simulation for a slab waveguide and a discussion of the band structure of the phononic crystal.

I. REPRESENTATION IN k-t SPACE

The standard form of the two-dimensional (2D) spatial Fourier transform is given by

$$F(\mathbf{k},t) = \frac{1}{(2\pi)^2}\int_{-\infty}^{+\infty}\int_{-\infty}^{+\infty} f(\mathbf{r},t)e^{-i\mathbf{k}\cdot\mathbf{r}}\,d^2\mathbf{r}, \tag{1}$$

where $\mathbf{r}$ is the position vector. When $f(\mathbf{r},t)$ does not contain counter-propagating waves, Eq. 1 is sufficient to provide the temporal evolution in $\mathbf{k}$-space. However, in the general case, $F(\mathbf{k},t)$ does not resolve into distinct positive and negative $\mathbf{k}$ components representing counter-propagating waves, since $F(\mathbf{k},t) = F^*(-\mathbf{k},t)$ (where * represents the complex conjugate). So if the standard 2D spatial Fourier transform of $f(\mathbf{r},t)$ is used, the resulting $\mathbf{k}$-space image $|F(\mathbf{k},t)|$ has inversion symmetry, clearly not the desired result for separating counter-propagating components of a general wave field.

In order to obtain a form for the $\mathbf{k}$-t-space amplitude that can be used to accurately represent the amplitudes of counter-propagating waves, first consider the spatiotemporal Fourier transform $F(\mathbf{k},\omega)$, where ω is the angular frequency, defined by

$$F(\mathbf{k},\omega) = \frac{1}{(2\pi)^3}\int_{-\infty}^{+\infty}\int_{-\infty}^{+\infty}\int_{-\infty}^{+\infty} f(\mathbf{r},t)e^{-i(\mathbf{k}\cdot\mathbf{r}-\omega t)}\,d^2\mathbf{r}\,dt. \tag{2}$$

In general, $F(\mathbf{k},\omega) \neq F^*(-\mathbf{k},\omega)$, because the extra temporal Fourier transform has resulted in the Fourier amplitude $F(\mathbf{k},\omega)$ now properly representing the amplitude of a wave propagating in the direction $\mathbf{k}$ (with frequency ω). The temporal evolution in $\mathbf{k}$-space for a single frequency ω can be expressed as $F(\mathbf{k},\omega)e^{-i\omega t}$. By defining

$$F_{\mathbf{k}}(\mathbf{k},t) = 2\int_0^{+\infty} F(\mathbf{k},\omega)e^{-i\omega t}d\omega, \tag{3}$$

we avoid ambiguity in the sign of $\mathbf{k}$ in $\mathbf{k}$-t space. No information is lost in this definition because $F(\mathbf{k},\omega) = F^*(-\mathbf{k},-\omega)$. As mentioned in the main text, in signal processing this representation is known as the analytic signal.[1]

II. SIMULATIONS

The experimental results are compared with a time-domain numerical simulation based on the finite element method (using PZFlex, Weidlinger Associates Inc.). The 3D model consists of a crystalline silicon substrate with a surface extending over 230 μm×230 μm and a depth of 100 μm, with crystal axes oriented as in the experimental sample. Absorbing boundary conditions are applied at the sides and bottom surface. The hole geometry is modelled as closely as possible to the sample, as shown in Fig. 1a–f of the main paper. The 50-nm top Cr film is also taken into account.

The thermoelastic laser excitation is represented by a simplified elastic-dipole model[2] that makes use of a radially-directed horizontal force with a spatial distribution given by re^{-r^2/d^2} applied over a circular region with a radius of 2 μm, where r is the radius and $d = 1$ μm. The temporal variation of the excitation is a steplike function (a quarter period of a sinusoid) with a 1 ns rise time. This produces a distribution of phonon wavevectors $\mathbf{k}$ that matches that in experiment.

The program gives the instantaneous velocity at each node at each time step, from which animations of duration 37.2 ns—equivalent to three cycles of the experimental data—were obtained. By superposing delayed versions of the phononic field, one can simulate the arrival of pulses at the laser repetition period, in our case at 0 ns, 12.4 ns and 24.8 ns.

The model consists of 290 million nodes (corresponding to 8.7×10^8 degrees of freedom) for the straight waveguide and 570 million nodes (corresponding to 1.7×10^9 degrees of freedom) for the lower-symmetry L waveguide. The accuracy of the simulation was checked by using different discretisations. The sample is reproduced on an orthogonal grid with elements of dimensions $0.16 \times 0.16 \times 0.16$ μm^3 ($\delta x \times \delta y \times \delta z$) at the top. The vertical dimension of the elements is gradually increased to $\delta z \approx 0.56$ μm at the bottom of the substrate. The temporal discretization of the model (6 ps) is chosen for numerical stability, and is derived from the smallest element dimension and the maximum wave velocity.[3] Since this high temporal resolution is unnecessary for the acoustic frequencies investigated, we only save data for every 15th time step (corresponding to a ∼90 ps effective time resolution). The simulations were carried out on the University of Strathclyde High Performance Cluster with parallel processing across 4 CPUs with 12 compute cores, and solutions were obtained in ∼100 hours.

Figure S1 shows the simulated evolutions in $\mathbf{k}$-space in the same format as the experimental data in Fig. 2 of the main paper. Full animations are also provided (see Section III). The results show good agreement with experiment.

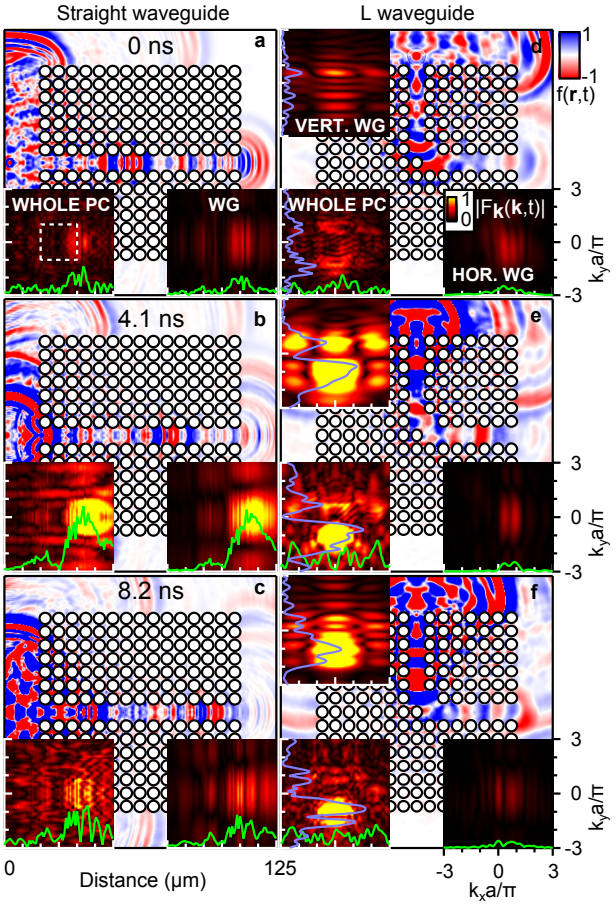

FIG. S1: Simulations of wave packet evolution in real space and **k**-space. (a)–(c) and (d)–(f) show snapshots taken at different delay times for the straight and L waveguides (WG), respectively, at 4.1 ns intervals. The insets of each image show the 2D **k**-space representation for the whole phononic crystal (PC) region and for the waveguide region at the corresponding time. The scales for the different times are identical for each type of plot. The scales for the vertical and horizontal sections of the L waveguide are also identical. The green curves are k_y=0 sections through the centre of the guide and, for the L waveguide, the purple curves (plotted with the origin on the right of the graphs) are equivalent k_x=0 sections. The white square in (a) shows the 1st Brillouin zone of the phononic crystal. The black circles represent the hole positions. Animations of these data and the corresponding experimental data are available.

For example, the frequency with the strongest transmission is 322 MHz. For the straight waveguide, we observe a peak in **k**-space around $k_x a/\pi = 0.8$. In the L waveguide, the slowly decaying peak observed in the experimental data in the horizontal section around $k_x a/\pi = 0.8$ is also present in the simulation. Some differences, for example a somewhat lower transmission to the horizontal branch (∼15%) can be ascribed to deviations from the sub-surface experimental geometry.

III. ANIMATIONS IN REAL SPACE, k-SPACE AND ENERGY SPACE.

We include animations for both experiment and simulation for the straight and L waveguides, as well as for simulations of a "slab-like" (non-PC) waveguide, discussed later in Section V, for comparison. The larger images are the real-time data in real space, showing waves being excited and propagating through the waveguides. The circles are drawn in to illustrate the hole positions. The real-space images have dimensions 125 μm×125 μm, as shown schematically in Fig. S2. The insets for each animation show **k**-t-space images (see Section I) for different regions of the samples.

Details of the sizes of the regions and sections used for both the experimental analysis and the simulations are given here, both for the **k**-t-space images and profiles thereof and for the animations. For the straight waveguide animations

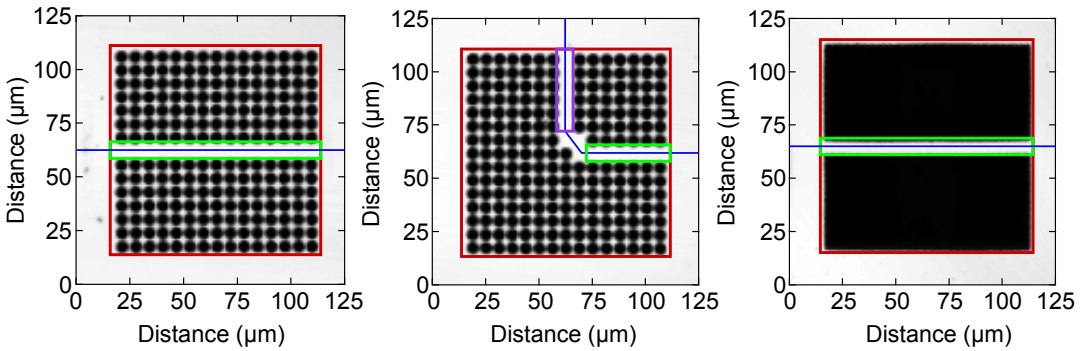

(a) Straight waveguide (b) L waveguide (c) Slab waveguide

FIG. S2: Regions used for **k**-space analysis. The blue lines show the cuts selected for sampling profiles of the acoustic field in the waveguides. (The diagonal blue line in (b) is not used for the cross-sections in Fig. 3 in the main text.)

and in Figs. S1a-c and 2a-c of the main paper, the left-hand **k**-space images (labelled "WHOLE PC") represent the square region containing all the holes, indicated by the red square in Fig. S2a; the right-hand **k**-space images (labelled "WG") represent the ∼92 μm ×7 μm waveguide region, indicated by the green rectangle in Fig. S2a; and the green curves in these animations and figures are profiles taken along the $k_y = 0$ axes of the **k**-space amplitude $|F(\mathbf{k}, \omega)|$ (see blue line in Fig. S2a). For the L-waveguide animations and in Figs. S1d-f and 2d-f of the main paper, the bottom-left **k**-space images again represent the square region containing all the holes, indicated by the red square in Fig. S2b; the right-hand **k**-space images (labelled "HOR. WG") represent the ∼37 μm ×7 μm horizontal section of the waveguide, indicated by the green rectangle in Fig. S2b; and the top **k**-space images (labelled "VERT. WG") represent the ∼7 μm ×37 μm vertical section of the waveguide, indicated by the purple rectangle in Fig. S2b. The green curves in these animations and figures are profiles taken along the $k_y = 0$ axes of the **k**-space amplitude $|F(\mathbf{k}, \omega)|$, and the purple curves are the corresponding profiles taken along the $k_x = 0$ axes (see blue lines in Fig. S2b).

For the straight waveguide we present an animation of the data of Fig. 4c in the main text for $+k_x$-directed waves as a function of frequency or, equivalently, phonon-energy using the relation $E = \hbar\omega$. One can see that, in line with the general increase in the spatial decay constant γ with frequency, the higher energies are more attenuated as the newly generated phonon wave packet (at t=0) traverses the waveguide. In addition, three peaks are clearly visible, corresponding to the three guiding peaks in Fig. 4a of the main paper. A very similar behavior is also seen for the corresponding simulation results, shown in the same animation on the right.

IV. SPATIOTEMPORAL FOURIER ANALYSIS

As discussed in the main text, frequency-filtered images in both real and **k**-space may be obtained by temporal and spatial Fourier transforms. $F_\omega(\mathbf{r}, \omega)$ was derived as follows:

$$F_\omega(\mathbf{r}, \omega) = \frac{1}{\sqrt{2\pi}} \int_{-\infty}^{+\infty} f(\mathbf{r}, t) e^{i\omega t} dt. \tag{4}$$

Figures S4–S6 show a more complete set of plots of A=$|F_\omega(\mathbf{r}, \omega)|$ at different frequencies for both experiment and simulation for the straight, L and slab waveguides. It is clear that 322 MHz is the frequency at which the phonons are guided most efficiently by the straight and L waveguides.

The dispersion relations in the main text were extracted from the real-time data using the spatiotemporal Fourier transform as in Eq. (2).

We have also derived the acoustic frequency spectrum from temporal Fourier transforms of a region of the sample not influenced by the PC waveguide. This spectrum is shown in Fig. S3.

V. SLAB WAVEGUIDE

The transmission of waves in a phononic crystal waveguide depends on both the wave leakage out of the waveguide and their scattering at the periodic waveguide walls. For comparison with a waveguide with neither of these effects,

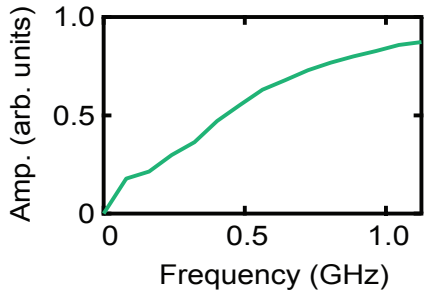

FIG. S3: The acoustic frequency spectrum derived from a region of the sample not influenced by the phononic crystal.

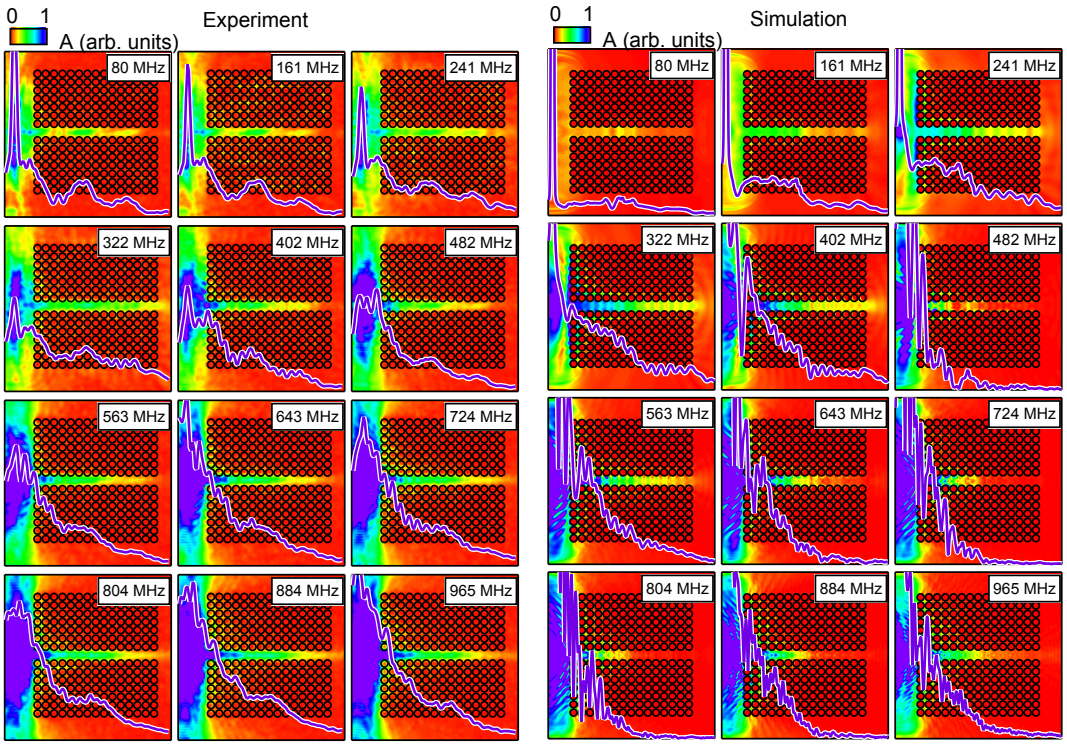

FIG. S4: Frequency-filtered images for the straight waveguide. Experimental (left) and simulated (right) images of $A=|F_\omega(\mathbf{r},\omega)|$. The purple curves are cross-sections through the centre of the waveguide, shown by the blue line in Fig. S2a. The images have dimensions 125 μm$\times$125 μm, and the scales for each set of images are identical.

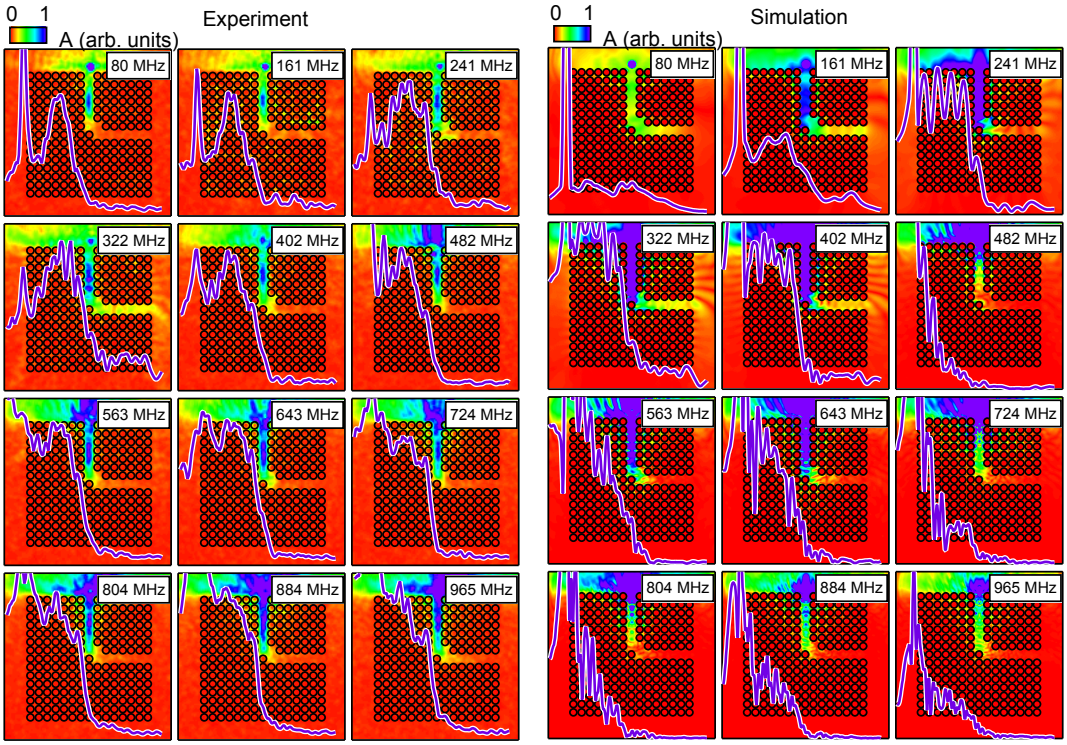

FIG. S5: Frequency-filtered images for the L waveguide. Experimental (left) and simulated (right) images of $A{=}|F_\omega(\mathbf{r},\omega)|$. The purple curves are cross-sections through the centre of the waveguide, shown by the blue lines in Fig. S2b. The images have dimensions 125 μm×125 μm, and the scales for each set of images are identical.

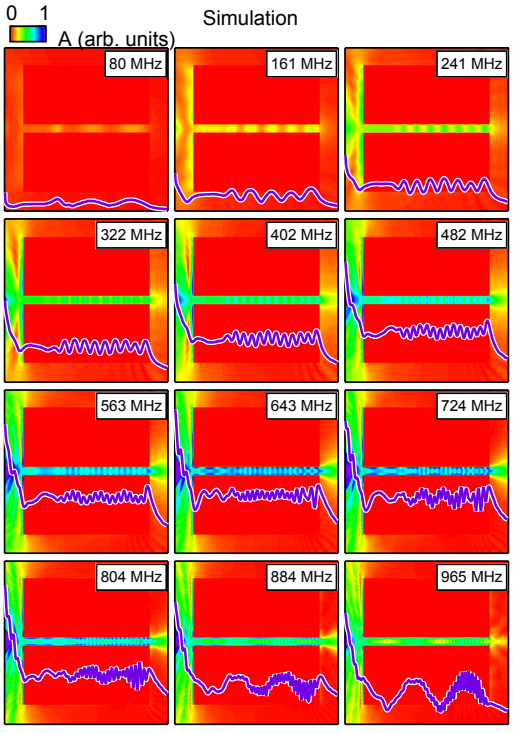

FIG. S6: Simulated frequency-filtered images for the slab waveguide. Images of $A{=}|F_\omega(\mathbf{r},\omega)|$ are shown for the case of a single pulse travelling through the waveguide. The purple curves are cross-sections through the centre of the waveguide, shown by the blue line in Fig. S2c. The images have dimensions 125 μm×125 μm, and the scales are identical.

we simulated a silicon "slab" waveguide (with no periodicity) of dimensions ∼95 μm × 6.3 μm, similar to that of the straight waveguide in this study in size and crystal orientation, and likewise connected at both ends to the bulk.. The acoustic source in the simulation is the same as that used for the straight waveguide. The real-time wave propagation is shown in animation form, as described in Section III. For this slab waveguide, the surface phonons are effectively confined to the waveguide near-surface region at all frequencies. Figure S7 shows the dispersion relation for the same range of k_x as used for the phononic crystal waveguides. The shape of the profile of $|F(\mathbf{k},\omega)|$ taken along the dispersion relation, shown below the main graph in Fig. S7, represents the excited wavevector distribution. At high frequencies, a branch from symmetrical Lamb waves propagating in the slab appears. The result of this can be seen in Fig. S6 above 884 MHz by the appearance of spatial beating. This effect is not seen in the PC waveguides.

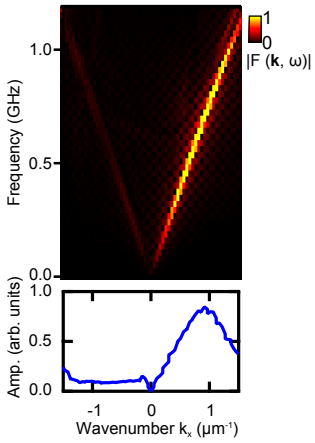

FIG. S7: Spatiotemporal Fourier-transform analysis for the slab waveguide from simulations. Dispersion relation for the slab waveguide, and (below) profile of $|F(\mathbf{k},\omega)|$ taken along the dispersion relation.

VI. BAND STRUCTURE OF THE PHONONIC CRYSTAL

For certain phononic crystal structures, such as phononic crystal plates, a complete band-structure calculation can be performed using the plane-wave expansion method[4]. Here the dispersion relations are influenced by many factors that complicate such calculations, such as anisotropy, acoustic leakage to the bulk, and sub-surface structure, as described by Fig. 1c-f. Because of this complex semi-infinite structure, we have at present no reliable analytical or numerical tool to generate a band structure. However, we have demonstrated in this paper that time-domain simulations are in reasonable agreement with experiment, and our results point to possible phononic stop or deaf bands in the regions near 320, 640 and 960 MHz.

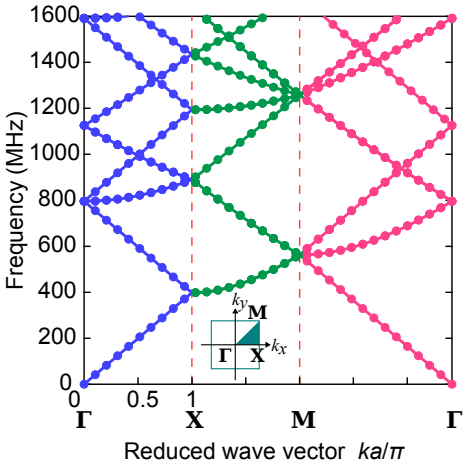

FIG. S8: Empty lattice model. Representation of the dispersion relation in the reduced-zone scheme of a square-lattice phononic crystal, assuming a constant velocity of 5 km/s and a lattice constant of 6.2 μm.

A first approximation of the dispersion relation for waves travelling in a periodic medium is the Empty Lattice Model[5]. This represents the limiting case when the size of the periodic defects approach zero. Figure S8 shows the dispersion relation of an isotropic square empty lattice with a wave velocity of ∼5 km/s, approximating to the Rayleigh wave velocity in silicon. In the case of very weak perturbations, band gaps open up at the Brillouin-zone boundaries; for example, a gap in the $\Gamma - X$ direction would appear near 400 MHz, or $k_x = 0.5\ \mu\text{m}^{-1}$. Although an interesting limiting case, the empty-lattice model is not, however, a reliable means of predicting band-gap positions in a phononic crystal with strong scatterers as in this paper.

---

[1] J. Smith *Mathematics of the Discrete Fourier Transform (DFT) with Audio Applications* (W3K Publishing, http://books.w3k.org/, 2007).
[2] I. Arias and J. D. Achenbach Int. J. Sol. Struct. **40**, 6917 (2003).
[3] K.-J. Bathe *Finite Element Procedures* (Prentice-Hall, Upper Saddle River, New Jersey, 1996).
[4] Y. Tanaka and S. Tamura. Phys. Rev. B **58**, 7958 (1998).
[5] C. Kittel *Introduction to Solid State Physics* (Wiley, New York, 2005).